Domain-wall dynamics driven by short pulses along thin ferromagnetic strips: Micromagnetic simulations and analytical description

Eduardo Martinez,[1,*] Luis Lopez-Diaz,[2] Oscar Alejos,[3] Luis Torres,[2] and Mario Carpentieri[4]
[1]*Universidad de Burgos, Plaza Misael Banuelos s/n, E-09001 Burgos, Spain*
[2]*Universidad de Salamanca, Plaza de la Merced s/n, E-37008, Salamanca, Spain*
[3]*Universidad de Valladolid, Prado de la Magdalena s/n, E-47005 Valladolid, Spain*
[4]*University of Calabria, Via P. Bucci, 42C I-87036 Arcavacata di Rende, Italy*
(Received 10 November 2008; revised manuscript received 26 January 2009; published 31 March 2009)

Micromagnetic simulations are used to describe the domain-wall dynamics along thin ferromagnetic strips driven by short pulses of magnetic field or electrical current with sinusoidal shape. For perfect strips without pinning centers, the net displacement of the domain wall is proportional both to the amplitude and the duration of the field pulse. A similar behavior is observed under current pulses if some nonadiabatic corrections are taken into account. On the contrary, the net displacement is null in the perfect adiabatic case. The domain-wall dynamics driven by these pulses is also characterized for strips which contain a single constriction, which acts as pinning site for the wall. The results reveal that an initially pinned domain wall can be eventually expelled far away from the constriction but if the maximum displacement does not surpass a given threshold the domain-wall experiences an attractive force which pushes it again toward the initial pinning site. Finally, the analysis of the domain wall jumps between two pinning sites is carried out both at zero and at room temperature for several separations between them. The simulations point out that the jumps can be achieved by means of short field or current pulses in the subnanosecond regime, an observation which could find application for a fast and easily controlled writing mechanism for future magnetic random access memory devices based on a pinned domain wall.

DOI: 10.1103/PhysRevB.79.094430 PACS number(s): 75.75.+a, 75.40.Mg, 75.40.Gb, 75.10.Hk

I. INTRODUCTION

In recent years, static and dynamics properties of domain walls (DWs) along thin ferromagnetic strips have attracted a great deal of attention due to their fundamental interest and their potential technological applications such as ultrahigh-density magnetic storage[1–6] and logic devices.[7,8] The success of these applications depends entirely on our ability to control accurately the domain-wall motion (DWM) along ferromagnetic strips. The traditional way to move a DW is by applying a magnetic field.[9–16] On the other hand, since the appearance of the work by Berger[17–19] and Slonczewski,[20,21] considerable effort has been put in understanding current-driven DWM.[16,22–33] Several works have experimentally analyzed the DWM driven by long static magnetic fields[13,15] and direct currents (dc).[34–41] For instance, the experimental measurements of the DW velocity carried by Atkinson *et al.*[13] under static fields could be explained as the balance between local pinning force due to the surface roughness and thermal fluctuations.[16] The experimental analysis by Meier *et al.*[39] on the current-driven DWM points out a stochastic nature of the DWM, which could originate from thermal effects of the joule heating[37,42] or local pinning due to roughness.[16,40] The current available theoretical descriptions of these experimental observation seems to indicate that some nonadiabatic corrections need to be taken into account but both the origin and the strength of the nonadiabaticity are still very controversial.[43,44]

The DW position along a ferromagnetic strip can be manipulated by means of a single constriction, which acts as a trap for the wall by locally lowering its magnetostatic energy.[45,46] The analysis of the depinning process driven by both static field and/or dc has been carried in several experimental[47–53] and theoretical[54] reports. It was also verified that the density current required to promote the DW depinning from a pinning site can be significantly reduced by means of oscillating currents (ac) when its frequency matches the natural frequency of the pinning site.[55–61]

In the present paper, the DW dynamics along thin Permalloy strips under the only action of short magnetic field or electric current pulses with sinusoidal shape is systematically investigated from a theoretical point of view. The paper is organized as follows. The geometries considered and the basic features of our micromagnetic simulations are presented in Sec. II. The DWM along a perfect strip (without pinning centers) driven by static magnetic field or electric current is reviewed in Sec. III A. After that, the DWM along a perfect strip driven by sinusoidal field and current pulses is micromagnetically analyzed in Sec. III B, and a one-dimensional model has been also used to complement the study. A similar strip but now containing a single pinning site is considered in Sec. IV. After that, the DW dynamics between two pinning sites under field or current pulses is micromagnetically studied in Sec. V. The same problem is also analyzed from a one-dimensional point of view in Sec. VI. Finally, the main conclusions of our work are presented in Sec. VII.

II. MICROMAGNETIC MODEL

The system under study consists of a thin Permalloy strip with $L_y \times L_z = 60 \times 3$ nm^2 cross section. A computational region of $L_x = 1.2$ μm in length was discretized by means of a standard finite-difference scheme using cubic computational cells of $\Delta x = 3$ nm inside. Figure 1 depicts the equilibrium

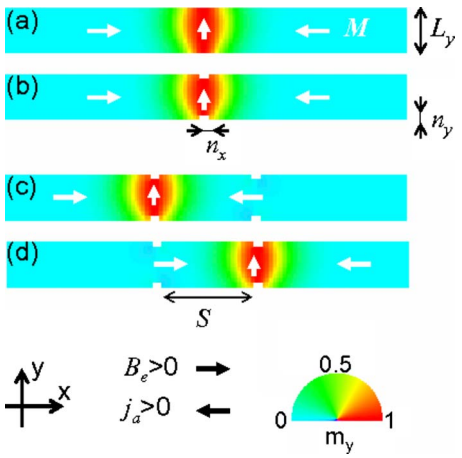

FIG. 1. (Color online) Equilibrium states of a head-to-head DW in absence of external field and current in (a) perfect strip and (b) strip with a single constriction. (c) and (d) show the two equilibrium states (at the left and at the right sites) for the DW in a strip with two identical constrictions, respectively. The cross section is $L_y \times L_z = 60 \times 3$ nm^2, and the notch dimensions are $n_x \times n_y = 15 \times 6$ nm^2. The sign criteria for the external field $B_e = \mu_0 H_e$ and the applied current j_a are also shown.

states of a head-to-head transverse DW at rest for three different cases: (a) a perfect wire (without pining centers), (b) a strip with a constriction which consists of two rectangular notches (15 nm long and 6 nm wide) symmetrically placed on both edges of the strip. Figures 1(c) and 1(d) depict the two possible equilibrium states of a DW pinned at one of the two identical constrictions separated $S=120$ nm. It has to be noted that in absence of driven force, and for dimensions and geometry here evaluated, the DW is symmetrically pinned in the center of the pinning sites.[54,61] The sign criteria for the positive fields and electrical density currents are also included in Fig. 1. Starting from these initial states, the dynamics of the local magnetization $\vec{M}(\vec{r})$ under the action of magnetic field pulses $\vec{B}_{\text{ext}}(t) = B_{\text{ext}}(t)\vec{u}_x$ or spin-polarized current pulses $\vec{j}_{\text{app}}(t) = j_{\text{app}}(t)\vec{u}_x$, both of them spatially uniform and directed along the strip axis (x axis), can be described by the extended Landau-Lifshitz-Gilbert equation as derived by Zhang and Li,[25]

$$\frac{d\vec{M}}{dt} = -\gamma_0 \vec{M} \times (\vec{H}_{\text{eff}} + \vec{H}_{\text{th}}) + \frac{\alpha}{M_s}\left(\vec{M} \times \frac{d\vec{M}}{dt}\right) + b_J(t)(\vec{u}_x \cdot \nabla)\vec{M} - \frac{c_J(t)}{M_s}\vec{M} \times (\vec{u}_x \cdot \nabla)\vec{M}, \quad (1)$$

where γ_0 is the gyromagnetic ratio, α is the Gilbert damping parameter, M_s is the saturation magnetization, and $\vec{H}_{\text{eff}}$ is the effective field, which includes exchange, self-magnetostatic, and external field contributions. $\vec{H}_{\text{th}}$ is the thermal field,[16] which is a Gaussian random process with the following statistical properties:[62,63]

$$\langle H_{\text{th},i}(\vec{r},t)\rangle = 0, \quad (2)$$

$$\langle H_{\text{th},i}(\vec{r},t) H_{\text{th},j}(\vec{r}',t')\rangle = 2D_{\mu M}\delta_{ij}\delta(\vec{r}-\vec{r}')\delta(t-t'). \quad (3)$$

The average of the thermal field taken over different stochastic realizations vanishes in each direction i in space (2). The thermal field $\vec{H}_{\text{th}}$ is assumed to be uncorrelated in time $[\delta(t-t')]$ and uncorrelated at different points $\delta(\vec{r}-\vec{r}')$ of the finite-difference mesh, as stated by Eq. (3). The strength of the thermal field, which follows from the fluctuation-dissipation theorem, is given by

$$D_{\mu M} = \frac{\alpha K_B T}{\gamma_0 \mu_0 M_s \Delta x^3}, \quad (4)$$

where Δx is the cell size, K_B is the Boltzmann constant, and T represents the temperature.

The last two terms on the right side of Eq. (1) represent the adiabatic and the nonadiabatic spin-transfer torques, respectively.[25] The coefficients $b_J(t)$ and $c_J(t)$ are given by $b_J(t) = j_{\text{app}}(t)\mu_B P/eM_s$ and $c_J(t) = \xi b_J(t)$, where μ_B is the Bohr magneton, P is the spin-polarization factor of the current, and $e<0$ is the electron's electric charge. The coefficient ξ is a dimensionless constant describing the degree of nonadiabaticity between the spin of conduction electrons and the local magnetization.[24] Typical Permalloy parameters were considered: saturation magnetization $M_s = 860$ kA/m, exchange constant $A = 13$ pJ/m, damping $\alpha = 0.02$, and polarization factor $P = 0.4$. All numerical details of our micromagnetic scheme can be found elsewhere.[16]

III. DW DYNAMICS ALONG PERFECT STRIPS

A. Static fields or currents

Let us first review the case of the DWM along perfect strips under static fields $[B_{\text{ext}} = B_e \neq f(t)]$ instantaneously applied at $t=0$. Starting from the initial state depicted in Fig. 1(a), the DWM is micromagnetically analyzed by numerically solving Eq. (1). Figures 2(a)–2(c) show the temporal evolution of the normalized DW width $[\Delta(t)/\Delta(0)]$, the DW position $[x(t)]$, and velocity $[v(t)]$ under two static fields (B_e) smaller than the so-called Walker field $(B_W = \mu_0 H_W = 6$ mT). $\Delta(0) \equiv \Delta_0 = 24.66$ nm is the value of the DW width at rest obtained from Thiele's definition. For $B_e < B_W$, the DW width relaxes exponentially, and it reaches a stationary value which decreases when B_e is augmented in the low-field range $(B_e < B_W)$. The snapshots of Figs. 3(a) and 3(b) show that the transverse DW state is preserved under static fields smaller than B_W, with a reduction in its width. At the same time, the DW velocity reaches a stationary regime, and therefore the DW position becomes a linear function of time. In this low-field regime, the terminal DW velocity increases with applied field as $v(\infty) = \gamma_0 \Delta(\infty) H_e/\alpha$, and as it is depicted in Fig. 2(g). For fields larger than the Walker breakdown, the wall moves with oscillations, and the average DW velocity drops. The snapshots of Fig. 3(c) reveal that the precession of the DW magnetization is spatially nonuniform. In fact, the precession from $+y$ to $-y$ DW magnetization occurs through the displacement, across the strip width and along the DW, of an antivortex with $+z$ core magnetization. Similarly, the conversion from $-y$ to $+y$ orientations occurs by the displacement

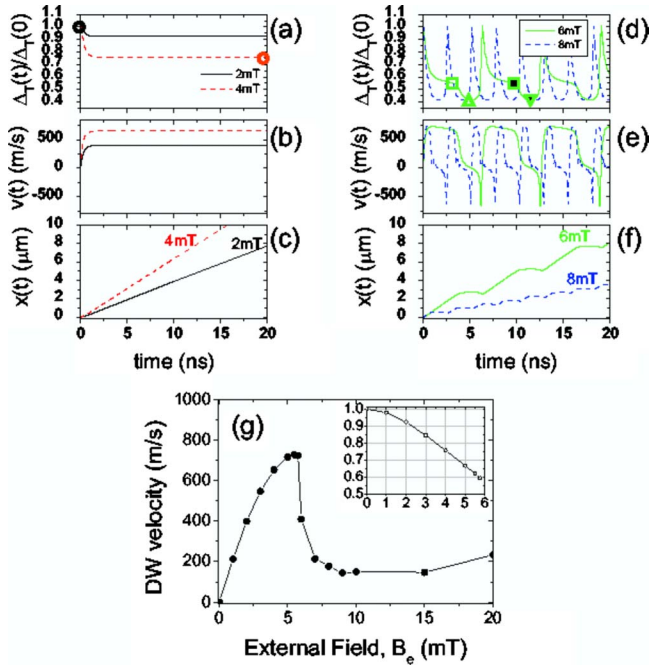

FIG. 2. (Color online) DW dynamics driven by static fields along perfect strips. (a)–(c) represent the temporal evolution of the DW width normalized to its static value $[\Delta(t)/\Delta(0)]$, the DW velocity $[v(t)]$, and the DW position $[x(t)]$ for two different static fields (2 and 4 mT) smaller than the Walker breakdown B_W. (d)–(f) represent the temporal evolution of the DW width normalized to its static value $[\Delta(t)/\Delta(0)]$, the DW velocity $[v(t)]$, and the DW position $[x(t)]$ for two different static fields, equal (B_e=6 mT) and larger (B_e=8 mT) than the Walker breakdown. The average DW velocity dependence on the applied field is shown in (g). The inset shows the stationary DW width $[\Delta(\infty)/\Delta(0)]$ as a function of field in the low regime ($B_e < B_W$).

of an antivortex with $-z$ core magnetization. This precessional DW motion has been already described from both theoretical[12,64] and experimental[15,65] studies. It has to be noted that the antivortex starts to nucleate in the strip edge at times around 2.6 ns for $B_e = B_W = 6$ mT, when the normalized

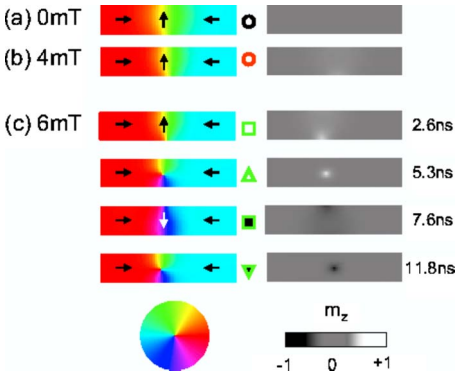

FIG. 3. (Color online) Micromagnetic snapshots of the DW state under static fields. (a) Equilibrium state at rest (B_e=0). (b) Stationary state reached under B_e=4 mT. (c) Snapshots of the DW states at different instants for B_e=6 mT. The color scale on the left pictures represents the in-plane magnetization, whereas the z component is coded from black (−1) to white (+1).

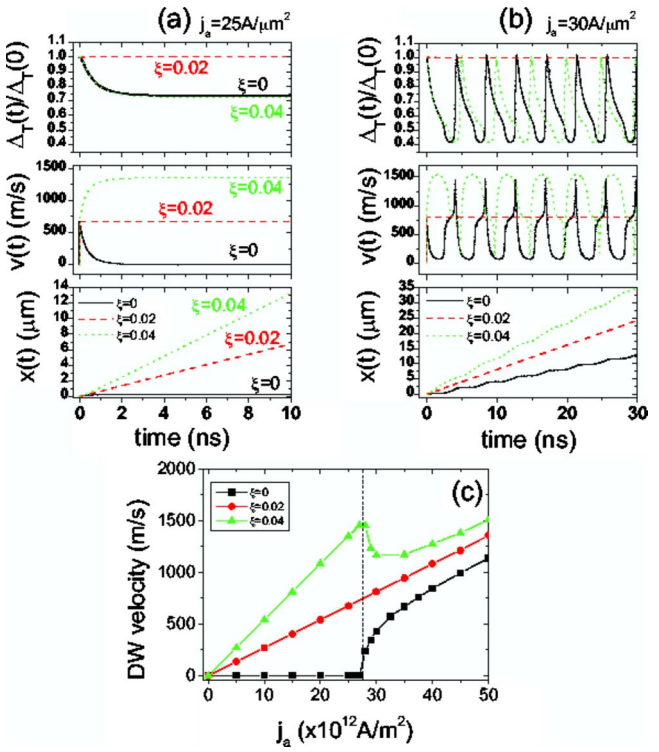

FIG. 4. (Color online) DW dynamics driven by static currents along perfect strips. (a) j_a=25 and (b) j_a=30 A/μm^2. (c) Averaged DW velocity as a function of j_a for different values of ξ.

DW width becomes smaller than $\Delta(t)/\Delta(0) \approx 0.6$ (that is, 40% smaller than its initial state). At t=5.3 ns, the antivortex is placed in the middle of the strip, and it has a representative DW width of $\Delta(t) \approx 0.4\Delta(0)$. Therefore, the presence of the antivortex can be monitored by the time evolution of the DW width: if the DW width reaches a value of $\Delta(t) \approx 0.6\Delta(0)$ or smaller, an antivortex starts to nucleate and move from the strip edge to the strip center, where it reaches its minimum width $[\Delta(t) \approx 0.4\Delta(0)]$. As the frequency of the DW transformation increases with B_e,[64,65] the time required for the DW transformation (from transverse to antivortex DW) decreases with B_e.[66]

The DW dynamics under static currents $[j_{app} = j_a \neq f(t)]$ is shown in Fig. 4 for three different values of the nonadiabatic parameter (ξ). For all cases, the adiabatic term (b_J) provides an initial DW velocity when the current is instantaneously applied at t=0. This initial DW velocity increases linearly with j_a as $v(0) = -b_J/(1+\alpha^2)$. As it is depicted in panel (a) of Fig. 4, for currents smaller than a given Walker-type threshold $[j_a < j_W(\xi)]$, which depends on ξ, the DW width relaxes to a new stationary value as the time elapses from t=0, and the initial DW velocity drops to zero if ξ=0. In this case, the final DW velocity is null, and the total displacement increases with j_a. If $\xi = \alpha = 0.02$, the DW structure does not change with respect to its static value when the current is turned on, and the DW velocity moves with constant terminal velocity $[v(\infty) = -c_J/\alpha]$. If $\xi = 2\alpha = 0.04$, the DW width relaxes again reaching a stationary value over a duration of $\approx$4 ns. Note that this change in $\Delta(t)$ is qualitatively similar to the one observed for ξ=0. However, the DW velocity

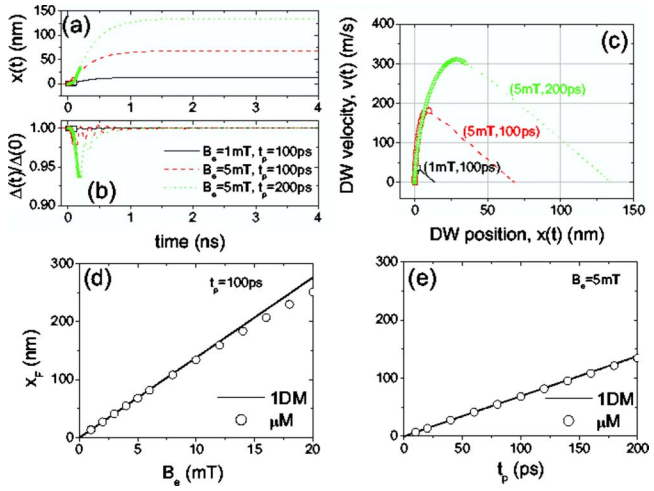

FIG. 5. (Color online) DW dynamics driven by sinusoidal field pulses along perfect strips. (a) and (b) show the micromagnetic results (μM) for DW position and width under pulses, different lengths t_p, and amplitudes B_e. (c) $v(t)$ versus $x(t)$ for the same pulses. Dots correspond to $t \leq t_p$, and lines correspond subsequent times ($t > t_p$). (d) Final DW position x_F reached by the DW for field pulses with different amplitudes (B_e) and constant length ($t_p = 100$ ps). (e) Final DW position x_F reached by the DW for field pulses with different lengths (t_p) and constant amplitude ($B_e = 5$ mT). In both (d) and (e), dots correspond to the micromagnetic results (μM), whereas lines represent the results predicted by the 1DM.

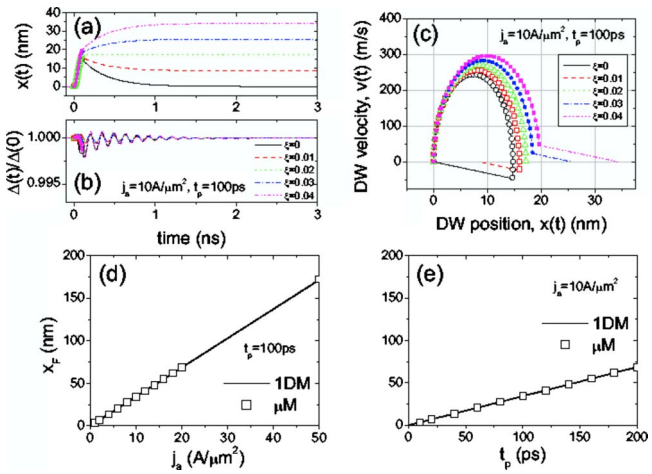

FIG. 6. (Color online) Micromagnetic results of DW dynamics driven by current pulses along perfect strips for different values of the nonadiabatic parameter ($0 \leq \xi \leq 2\alpha$). (a) and (b) show the micromagnetic results (μM) for the DW position and width under pulses of $t_p = 100$ ps and $j_a = 10$ A/μm^2, respectively. (c) DW velocity as a function of DW position. Dots correspond to $t \leq t_p$, and lines correspond to subsequent times ($t > t_p$). (d) and (e) show the final DW position x_F reached by the DW for different current pulses considering a nonadiabatic parameter of $\xi = 0.04$: (d) the length is constant ($t_p = 100$ ps) and j_a is varied; (e) the amplitude is fixed ($j_a = 10$ A/μm^2) and t_p is varied. In both (d) and (e), dots correspond to the micromagnetic results (μM), whereas lines correspond to the results predicted by the 1DM.

increases exponentially, and it reaches a new stationary value larger than the initial DW velocity.

When the current surpasses the Walker-type threshold $j_a \geq j_W(\xi)$ (which depends on ξ), the DW motion depicts some features similar to the high-field driven case: the wall moves with oscillations related to the DW transformations which occur through the injection and motion of an antivortex across the strip width.[26] Typical results are shown in right panel of Fig. 4(b). Except for the case of $\xi = \alpha$, the DW motion depicts oscillations which are related to DW transformations from transverse to antivortex and from this one to the first, and so on. This behavior is similar to the observed under static fields with one difference: under static currents, the instantaneous DW velocity is always positive. Due to the DW transformations for $j_a \geq j_W(0)$, a net DW velocity is obtained. The average DW velocity as a function on j_a is shown in Fig. 4(c) for three different values of ξ in agreement with other studies.[27]

B. Field or current pulses

In this section, we consider the DW response to the action of field pulses with sinusoidal form [$B_{\text{ext}}(t) = B_e \sin(\pi t/t_p)$ if $0 \leq t \leq t_p$, and $B_{\text{ext}}(t) = 0$ for $t \geq t_p$]. Starting from the initial state depicted in Fig. 1(a), the DWM is micromagnetically analyzed by numerically solving Eq. (1). Figures 5(a) and 5(b) show the temporal evolution of the DW position [$x(t)$] and normalized DW width [$\Delta(t)/\Delta(0)$] under several field pulses with different durations (t_p) and different amplitudes (B_e). The DW velocity as a function of the DW position is depicted in Fig. 5(c). The DW position increases monotonously during the pulse application but the DW velocity reaches a maximum some time before the pulse has been turned off. After that, the DW velocity is still positive, and therefore DW continues moving to the right from the initial position. For times larger than ≈ 3 ns, the DW finally stops. As shown in Fig. 5(b), the minimum value of the normalized DW width [$\Delta(t)/\Delta(0)$] does not become smaller than 0.6, and therefore, the transverse nature of the DW is preserved during these field pulses. The distance traveled by the DW increases linearly with both the pulse length (t_p) and the amplitude of the pulse (B_e), as shown in Figs. 5(d) and 5(e). All these micromagnetic results can be understood from a well-established one-dimensional model (1DM) that treats the DW as a rigid object (see Appendix), where the value of the DW width was obtained from the equilibrium state of Fig. 1(a) by using the Thiele definition ($\Delta_0 = 24.66$ m) (see Ref. 16 for details). The good quantitative agreement between micromagnetic results (μM, dots) and the 1DM predictions (lines) is evident in Figs. 5(d) and 5(e).

Figure 6 shows the micromagnetic results of the DWM induced by sinusoidal current pulses [$j_{\text{app}}(t) = j_a \sin(\pi t/t_p)$ if $0 \leq t \leq t_p$, and $j_{\text{app}}(t) = 0$ for $t \geq t_p$] for different values of the nonadiabatic parameter ($0 \leq \xi \leq 2\alpha$). The temporal evolution of $x(t)$ and $\Delta(t)/\Delta(0)$ is shown in Figs. 6(a) and 6(b), respectively. The velocity (v) as a function of the position (x) is depicted in Fig. 6(c). The length of the current pulse is $t_p = 100$ ps and its amplitude is $j_a = 10$ A/μm^2. As in the field-driving case, the DW position $x(t)$ increases from $t = 0$ to $t = t_p$. However, the evolution of the DW velocity $v(t)$ is quite

different than the one observed for the field-driving case. If the nonadiabatic parameter is smaller than the damping factor ($\xi<\alpha$), the DW velocity is negative at the end of the pulse [$v(t_p)<0$]. This behavior is similar to the one observed by Thiaville *et al.*[67] in strips of 120×5 nm^2 cross section, and for other different pulses in the low current amplitude regime. The minimum DW velocity at the end of the pulse is observed for the perfect adiabatic case ($\xi=0$) and it increases, becoming null if $\xi=\alpha=0.02$ [$v(t_p)=0$]. For $\xi>\alpha$, the $v(t_p)$ is positive, and it increases with both the length and the amplitude of the current pulses. When the pulse is turned off ($t\geq t_p$), the DW velocity relaxes to zero, and the DW position reaches a final value [$x_F\equiv x(t\gg t_p)$]. As it is shown in Fig. 6(c), the DW position decreases (increases) monotonously after the pulse if $\xi<\alpha$ (if $\xi>\alpha$), whereas it remains constant if $\xi=\alpha$. The micromagnetic results show that net displacement for times sufficiently larger than the current pulse duration [$x_F\equiv x(t\gg t_p)$] is zero in the perfect adiabatic case ($\xi=0$), and it increases linearly with $\xi>0$. The final position reached by the DW under current pulses of different amplitudes (j_a) and different durations (t_p) is depicted in Figs. 6(d) and 6(e), respectively, considering a nonadiabatic parameter of $\xi=0.04$. In the same manner as for the field pulses, the DW displacement increases linearly with both the amplitude j_a and the length t_p of the pulses, and the micromagnetic results (μM, open dots) are in good quantitative agreement with the 1DM (lines) predictions (see Appendix). Note that $\Delta(t)/\Delta(0)$ is well above that of the antivortex nucleation threshold value [$\Delta(t)/\Delta(0)\approx0.6$].

IV. DW DYNAMICS IN PRESENCE OF A SINGLE CONSTRICTION

In this section, we consider the same strip as from the above section but now containing a single pinning site which consists of two rectangular notches symmetrically patterned at both sides of the strip. The geometry analyzed is depicted in Fig. 7(a). Figure 1(b) shows the equilibrium state for notches with length $n_x=15$ nm and depth $n_y=6$ nm. It is important to note that for this particular strip geometry the DW is pinned in the center of the pinning site. The DW quasistatic depinning process from this pinning site has been already studied by our group.[54] Under static fields [$B_{\rm ext}(t)=B_e\neq f(t)$], the DW remains pinned inside the pinning potential for fields smaller than the depinning threshold ($B_{\rm dep}$). This quasistatic depinning threshold increases with the depth of the notches (n_y). For fields larger than the depinning threshold ($B_e>B_{\rm dep}$), the DW is depinned from the pinning trap, and it reaches a steady velocity for applied fields B_e smaller than the Walker breakdown. As it is observed in Fig. 7(b), the DW displacement $x_{\rm eq}(B_e)$ under static fields smaller than the critical depinning value ($B_e<B_{\rm dep}$) increases linearly with the field. As the field approaches the depinning threshold, the slope of $x_{\rm eq}$ as a function of B_e starts to increase, and it slightly deviates from the original linear rise. As it is shown in Fig. 7(b), both the length (L_N) and the depinning field ($B_{\rm dep}$) increase with the depth of the notches (n_y). The profile of the pinning potential [$V_{\rm pin}(x)$] induced by the constriction was computed from the total micromagnetic energy for each equilibrium state ($V_{\rm pin}=E_{\rm exch}+E_{\rm dmg}$, where $E_{\rm exch}$ and $E_{\rm dmg}$ are the exchange and magnetostatic contributions to the total micromagnetic energy). For $B_e<B_{\rm dep}$, $V_{\rm pin}(x)$ depicts a parabolic profile which extends over a distance of $L_N=16-21$ nm from the center of the constriction [see Fig. 7(c)].

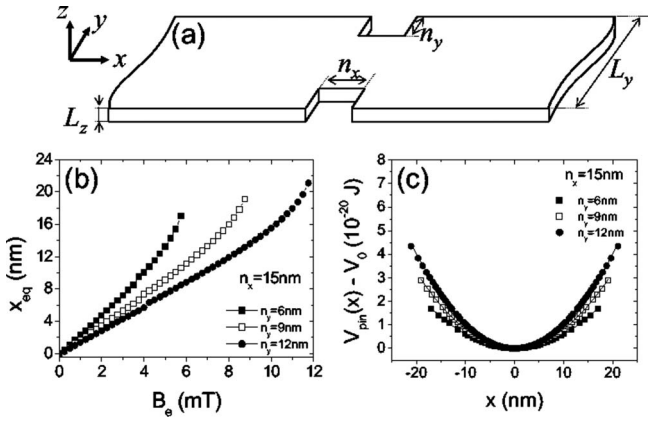

FIG. 7. (a) Schematic representation of the simulated geometry of a strip with a single pinning site consisting of two rectangular notches of length n_x and depth n_y. (b) DW equilibrium position as a function of the static field in the pinned regime inside the pinning site for strips of $L_y\times L_z=60\times3$ nm^2 with notches of $n_x=15$ nm and several depths n_y. (c) Pinning potential $V_{\rm pin}(x)$ as a function of the DW position.

Let us now analyze the micromagnetic results of the DW dynamics induced by field pulses with sinusoidal shape considering a constriction with $n_x=15$ nm in length and $n_y=6$ nm in depth. Starting from the initial state of Fig. 1(b), Fig. 8 shows the micromagnetic DW response to the action of field pulses of fixed length $t_p=100$ ps and several maximum amplitudes B_e. From Thiele's definition, the value of

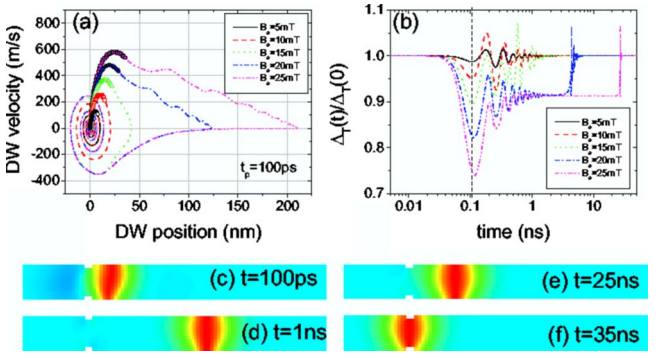

FIG. 8. (Color online) DW velocity as a function of the DW position driven by field pulses of constant length ($t_p=100$ ps) and different amplitudes in presence of a single pinning site with $n_x=15$ nm and $n_y=6$ nm. (a) and (b) show the temporal evolution of the DW position $x(t)$ and DW width $\Delta(t)$ for pulses with $B_e=5$ mT (solid black line), $B_e=10$ mT (dash red line), $B_e=15$ mT (dot green line), $B_e=20$ mT (blue dash dot line), and $B_e=25$ mT (pink dash dot dot line). Dots represent times during the pulse ($t\leq t_p$), whereas lines correspond to the subsequent free DW dynamics ($t>t_p$). (c)–(f) show the micromagnetic configurations at different instants for a pulse of $B_e=25$ mT and $t_p=100$ ps.

the width of this pinned DW at rest is $\Delta_0=21.14$ nm. As expected, both the DW velocity and the DW displacement at the end of the pulse increase with the field amplitude B_e. For instance, under a pulse of $B_e=15$ mT and $t_p=100$ ps [see green line in Figs. 8(a) and 8(b)], the DW position reaches a maximum value of 41.5 nm at $t=0.24$ ns. After that ($t>t_p$), the DW is attracted by the constriction, and it finally returns to its initial state after having developed free and damped oscillations. The frequency of these damped oscillations is ≈ 2.5 GHz, a value which agrees well with the one predicted by the 1DM.[54] A similar behavior is observed for more intense pulses [see blue and pink lines in Figs. 8(a) and 8(b)]. In these cases, the DW is displaced far away from the pinning site, over a distance several times larger than the physical size of the pinning site, which is given by n_x. In particular, Figs. 8(c)–8(f) show the DW state at different instants for a pulse of $B_e=25$ mT. At the end of the pulse the DW position $x(t_p)\approx 37$ nm, and the DW velocity $v(t_p)\approx 525$ m/s. Figure 8(c) show the micromagnetic configuration of the DW at $t=t_p$. After that ($t>t_p$), the DW continues moving away from the constriction up to $t\approx 1.88$ ns, where it reaches its maximum displacement from the center of the pinning site [$x(1.88\ \text{ns})\approx 210$ nm]. In this instant, the DW velocity starts to decrease reaching a minimum value of -352 m/s at $t=26.9$ ns. Therefore, the DW starts to be attracted again toward its initial position, which is finally reached at $t\approx 35$ ns [see Fig. 8(f)]. Note that the minimum value of the normalized DW width is reached approximately at the end of the pulse. But more importantly, even for these pulses with high maximum amplitude of $B_e=25$ mT, the wall width never becomes smaller than the antivortex injection threshold (≈ 0.6), and therefore, the transverse structure remains during the whole DW motion. These results indicate that the attractive pinning potential extends over a distance several times larger than the physical size of the constriction. It was also verified that the maximum displacement of the DW increases with both the duration (t_p) and the amplitude (B_e) of the pulse. For example, under a pulse of $B_e=25$ mT and $t_p=200$ ps the maximum displacement of the DW before returning to its initial state is 437 nm (at $t=2.89$ ns).

Although it is not displayed here, it was also observed that, if the length of the pulse with $B_e=25$ mT is increased to $t_p=500$ ps, the DW eventually adopts an antivortex configuration during the pulse. In this case, the DW reaches a final position at 860 nm from the center of the pinning site, where it finally recovers its transverse configuration, and it does not return to the initial state since, for such a large distance, the DW does not feel the magnetostatic pinning force induced by the constriction.

Figure 9 shows the micromagnetic results for the DW dynamics under current pulses of constant duration $t_p=100$ ps and different amplitudes j_a, by considering three different values of the nonadiabatic parameter: (a) $\xi=0$, (b) $\xi=0.02$, and (c) $\xi=0.04$. As expected, the maximum displacement reached by the wall at the end of the pulse [$x(t_p)$] increases with both j_a and ξ. For instance, under current pulses with $(j_a,t_p)=(60\ \text{A}/\mu\text{m}^2, 100\ \text{ps})$ (see green lines in Fig. 9), the DW velocity becomes negative before the end of the pulse ($t=t_p$) in the perfect adiabatic limit ($\xi=0$), and the

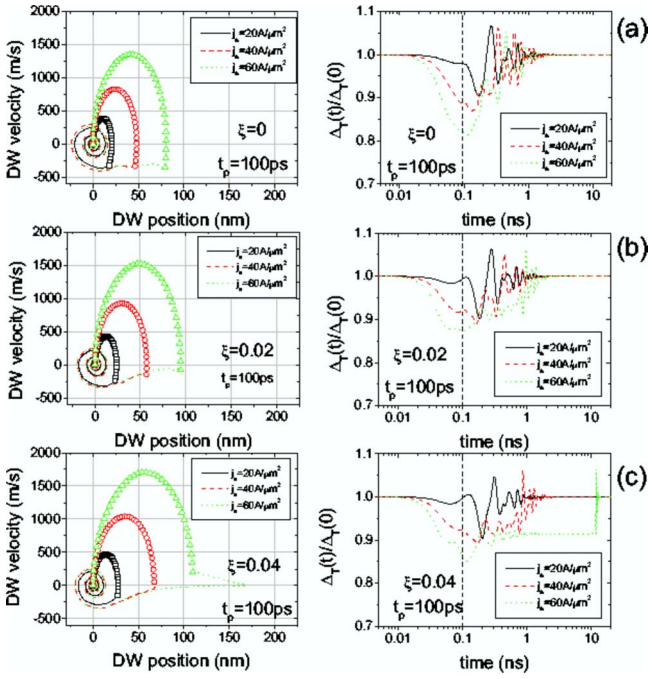

FIG. 9. (Color online) DW velocity as a function of DW position (left panel) and DW width as a function of time (right panel) under current pulses of constant length ($t_p=100$ ps) in presence of a single pinning site with $n_x=15$ nm and $n_y=6$ nm. From top to bottom: (a) $\xi=0$, (b) $\xi=0.02$, and (c) $\xi=0.04$. Each curve corresponds to different values of j_a: black lines—$j_a=20$ A/μm^2, red lines—$j_a=40$ A/μm^2, and green lines—$j_a=60$ A/μm^2. Dots on left panel represent the values during the pulse ($t\le t_p$), whereas lines correspond to the subsequent free DW dynamics ($t>t_p$).

DW returns to its initial state [see Fig. 1(a)] after damped oscillations. A similar behavior is also observed for $\xi=\alpha$ [see green lines in Fig. 9(b)]. However, if $\xi=2\alpha$, the DW velocity is still positive after the pulse is turned off [Fig. 9(c)]. Then, the DW velocity starts to decrease and the DW displacement reaches a maximum value of $x\approx 167$ nm at $t\approx 1.29$ ns. After that ($t>1.29$ ns), the DW starts again to be attracted to the pinning site. As it is shown in the right panel of Fig. 9, $\Delta(t)/\Delta(0)$ remains always larger than the antivortex nucleation threshold [$\Delta(t)/\Delta(0)\approx 0.6$] over the whole motion, a fact which indicates that the transverse structure of the wall is preserved over the whole process. As for the field-driven case, the maximum distance traveled by the DW is several times larger than the physical size of the pinning site, and it is also larger than the length of the pinning potential $L_N\approx 20$ nm quasistatically computed [see Fig. 7(b)]. Based on these micromagnetic results, the constriction induces a position dependent pinning potential $V_{\text{pin}}(x)$ of magnetostatic nature, which can be described by a restoring elastic force $F_p(x)=-\partial V_{\text{pin}}(x)/\partial x=-K_N x$ if $|x|\le L_N$. For $L_N<|x|<L_N'$ (where $L_N'\approx 30n_x$), although the position x is larger than the physical size of the constriction ($n_x=15$ nm), there is still a net force on the DW which attracts it toward the center of the pinning potential ($x=0$). Only at distances further than $|x|>L_N'$ does the DW not experience any attractive force from the constriction.

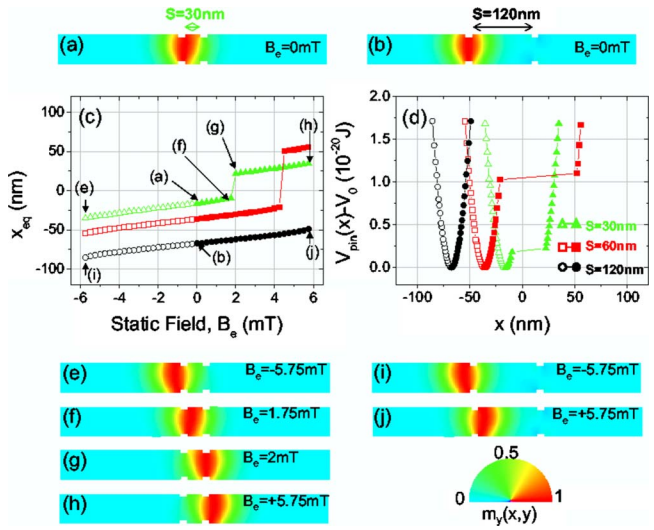

FIG. 10. (Color online) Equilibrium states of the DW in a strip with two pinning sites under static fields in the pinned regime.

V. DWM BETWEEN TWO PINNING SITES

The simulations of former sections indicate that the energy barrier of a trapped DW inside a single pinning site can be controlled by the depth of the constriction, and that a DW can be eventually displaced from it by means of fast field and current pulses in the subnanosecond regime. In this section, and in order to analyze the DW transitions between two pinning sites, a strip with $L_y \times L_z = 60 \times 3$ nm^2 containing two identical constrictions with $n_x \times n_y = 15 \times 6$ nm^2 is considered. In absence of any driving force, the DW is pinned at one of two equilibrium states of a double-potential well. Figures 1(c) and 1(d) show these two states, where the constrictions are separated $S=120$ nm from each other. Figure 10(a) depicts the equilibrium state at zero field of the DW pinned in the left pinning site, which is separated from right pinning site by $S=30$ nm. Contrary to the case of similar notches but at $S=120$ nm from one another [see Fig. 10(b)], the DW is not symmetrically placed in the center of the notch when $S=30$ nm. In this case, the DW is slightly displaced toward the pinning site on the right. In order to describe the influence of the separation between the pinning sites on the pinning potential, we analyzed the quasistatic pinning regime under static fields with two similar pinning sites at different separations (S). Figure 10(c) shows the DW equilibrium position x_{eq} as a function of static fields $[B_{\mathrm{ext}}=B_e \neq f(t)]$ in the pinned regimen for three different values of S. At zero field, the DW is placed in the left pinning site (at $x=x_L<0$). It is noted that by forcing the DW depinning toward negative positions driven by negative fields ($B_e<0$), the minimum field needed to promote does not depend on S. However, the positive field required to promote the DW jump from the left pinning site (at $x_L<0$) to the right (at $x_R>0$) is strongly influenced by the separation S. If distance between pinning sites decreases under a given threshold, the pinning potential of both notches overlap around the central point ($x=0$), and this results on a reduction in the energy barrier between them, as can be noted in Fig. 10(d), which depicts the micromagnetically deduced pinning profile. In particular, a field of 2 mT is enough to produce the jump of the DW to the right pinning site if $S=30$ nm. For fields 2 mT$\leq B_e \leq 5.75$ mT$=B_{\mathrm{dep}}$, the DW remains trapped in the right pinning site, and if the field surpasses this depinning threshold value, the DW is depinned, and it continues moving. The snapshots depicted in Figs. 10(a) and 10(e)–10(h) represent the equilibrium magnetization texture at different static fields for $S=30$ nm. A similar behavior is observed if $S=60$ nm but a larger field of 4.5 mT is required for the DW jumping from the left to the right pinning site. On the contrary, if the separation rises to $S=120$ nm, a minimum field of 6 mT is required to expel the DW from the left pinning site, and the DW is not trapped in the right pinning site. Some equilibrium states for $S=120$ nm are depicted in Figs. 10(b), 10(i), and 10(j). This analysis indicates that the energy barrier between two pinning sites can be controlled by changing the separation between them, and therefore, it could be useful for application on memory devices where the thermal stability of a magnetic bit is determined by the ratio between the energy barrier E_B to the thermal energy K_BT.

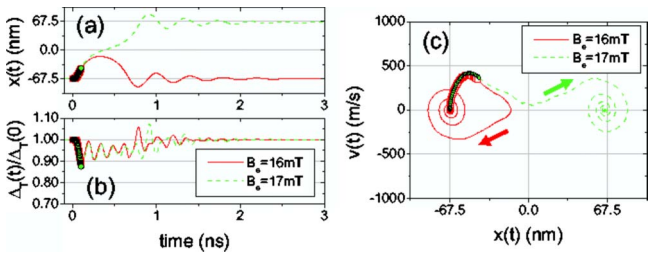

FIG. 11. (Color online) DW dynamics between two pinning sites separated by $S=120$ nm. Temporal evolution of (a) the DW position and (b) the DW velocity under two field pulses of fixed duration ($t_p=100$ ps) with two amplitudes: $B_e=16$ mT (red line) and $B_e=17$ mT (blue line). (c) Trajectories in the phase space $[v(t)$ vs $x(t)]$ corresponding to the same field pulses. The duration of the pulse is also $t_p=100$ ps, and the amplitude j_a is given on the graphs. Dots correspond to times $0 \leq t \leq t_p$, whereas lines show the subsequent free DW dynamics ($t > t_p$).

Let us focus on the DW dynamics driven by field pulses in a strip containing two similar notches which are separated $S=120$ nm from each other. Starting from the initial state of Fig. 1(c) or Fig. 10(b), where the DW is pinned at the center of the left pinning site $[x(0)=x_L \equiv -67.5$ nm], micromagnetic simulations are used to describe the DW dynamics. Our aim here is to determine the critical amplitude (B_e or j_a) and the critical duration (t_p) of pulses needed to promote the jump toward the pinning site at the right ($x_R=+67.5$ nm).

The micromagnetically computed response of this pinned DW [initially in the left pinning site, at $x(0)=x_L=-67.5$ nm] to the action of two field pulses of constant duration ($t_p=100$ ps) and two different amplitudes ($B_e=16$ mT and $B_e=17$ mT) is depicted in Figs. 11(a) and 11(b), which show the temporal evolution of both the DW position $x(t)$ and the DW width $\Delta(t)/\Delta(0)$, respectively. Figure 11(c) shows the DW trajectory in the phase domain $[v(t)$ vs $x(t)]$ for the same field pulses. For both pulses, the DW position increases during the pulse application ($0 \leq t \leq t_p$) from $x(0)=x_L$ toward $x=0$, which represents the center of the potential landscape, and the DW velocity reaches a maxi-

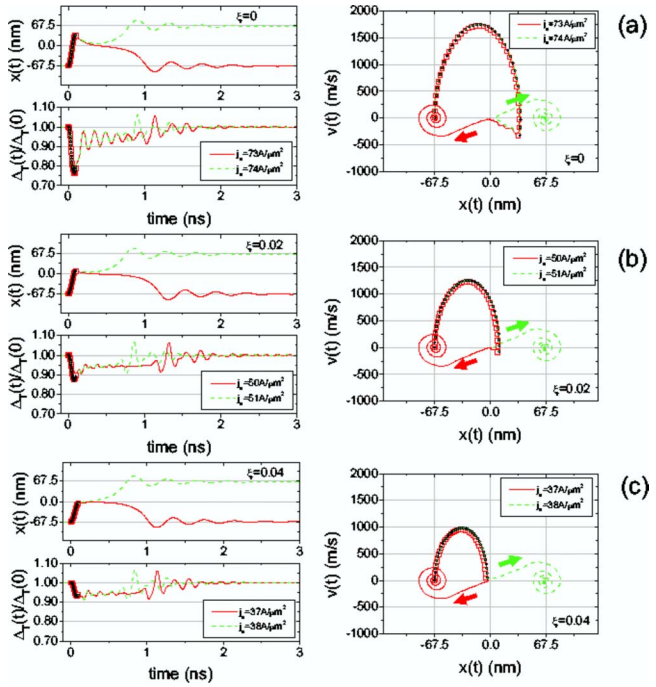

FIG. 12. (Color online) DW dynamics between two pinning sites separated by $S=120$ nm driven by current pulses: (a) $\xi=0$, (b) $\xi=0.02$, and (c) $\xi=0.04$. On the left panel, the DW position and the DW width are represented as a function of time. Right panels depict the DW velocity as a function of the DW position. The duration of the pulse is also $t_p=100$ ps, and the amplitude j_a is given on the graphs. Dots correspond to times $0\leq t\leq t_p$, whereas lines show the subsequent free DW dynamics ($t>t_p$).

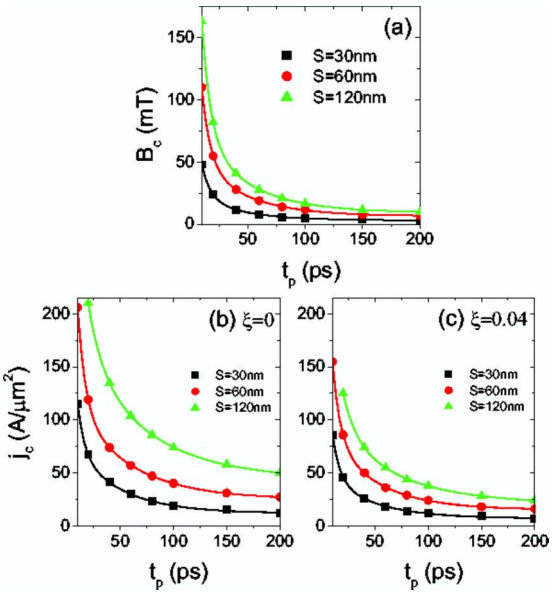

FIG. 13. (Color online) Critical amplitudes of the (a) field (B_c) and current (j_c) pulses, and (b) $\xi=0$ and (c) $\xi=2\alpha=0.04$ as a function of the duration t_p. Three different separations between the constrictions are considered: $S=30$ nm (black squares), $S=60$ nm (red circles), and $S=120$ nm (green triangles). Lines are guides for the eyes.

mum value at $t\approx 90$ ps. After that, the DW velocity decreases freely. For $B_e=16$ mT, the DW velocity becomes negative before it has reached the central point ($x=0$) of the double-potential well, and it starts to be attracted toward the initial state [Fig. 1(c)]. On the contrary, if $B_e=17$ mT the DW reaches the central point of the potential landscape ($x=0$) with positive velocity, and it starts to be attracted toward the pinning site on the right ($x_R=+67.5$ nm).

Figures 12(a)–12(c) depict the critical trajectories of the DW in the phase space [$v(t)$ vs $x(t)$] under two current pulses of fixed duration ($t_p=100$ ps) and different amplitudes (j_a), for $\xi=0$, $\xi=\alpha=0.02$, and $\xi=2\alpha=0.04$ cases, respectively. In the perfect adiabatic case ($\xi=0$) [see panel (a) in Fig. 12], the DW surpasses the central point $x=0$ during the pulse application but the DW velocity becomes negative before the pulse has been turned off. The minimum value (more negative) of the velocity is reached at the end of the pulse. For $j_a=73$ A/μm^2, $v(t_p)\approx -339$ m/s, whereas $v(t_p)\approx -337$ m/s for $j_a=74$ A/μm^2. After that ($t\geq t_p$), the DW relaxes freely in the pinning potential. For $j_a=73$ A/μm^2, the DW crosses backward over the central point (from $x>0$ to $x<0$) with negative velocity, and therefore, after damped oscillations it returns again to the left pinning site ($x_L=-67.5$ nm). If the amplitude of the pulse increases to $j_a=74$ A/μm^2, the DW velocity becomes positive before crossing the middle point of the double-potential well, and it finally becomes pinned at the right pinning site ($x_L=+67.5$ nm). A similar behavior is observed for $\xi=0.02$ [see panel (b) in Fig. 12], but now, the critical amplitude ($j_c=51$ A/μm^2) for the DW jump is reduced with respect to the former case ($\xi=0$). The critical trajectories for $\xi=2\alpha=0.04$ are depicted in panel (c) of Fig. 12. In this case, the DW does not cross over the central point of the double pinning well at the end of the pulse, that is, $x(t_p)<0$. If $j_a=37$ A/μm^2 the DW velocity becomes negative after the pulse ($t>t_p$), and the DW returns to the initial state. However, for a pulse with $j_a=38$ A/μm^2, the DW velocity is still positive at $t=t_p$ and after that, the DW crosses over $x=0$, and it becomes attracted to the pinning site on the right [$x=x_R$, see Fig. 1(d)], where it is finally trapped. As it is clear in both Figs. 11 and 12, the normalized DW width $\Delta(t)/\Delta(0)$ remains well above the antivortex injection threshold (≈ 0.6), and therefore, the transverse configuration of the DW is preserved during both the field and current jumps.

In order to determine how the critical amplitude of the pulse (B_c or j_c) depends on its duration (t_p), a systematic analysis of the DW dynamics was carried out for several separations S between both pinning sites. The results are collected in Fig. 13(a) for field pulses, and in Figs. 13(b) and 13(c) for current pulses considering $\xi=0$ and $\xi=0.04$, respectively. For combinations of (B_e,t_p) or (j_a,t_p) above (below) each curve, the jump from the left to the right pinning takes place (does not take place). As it was expected from former observations, for a given length t_p, the minimum amplitude of the pulse needed to promote the DW jump to the adjacent constriction increases with S, and both B_c or j_c decrease when the pulses are longer.

Former micromagnetic results were computed at zero temperature. In order to get a more realistic description, the DW jumps under both sinusoidal field and current pulses were analyzed at room temperature $T=300$ K for a separa-

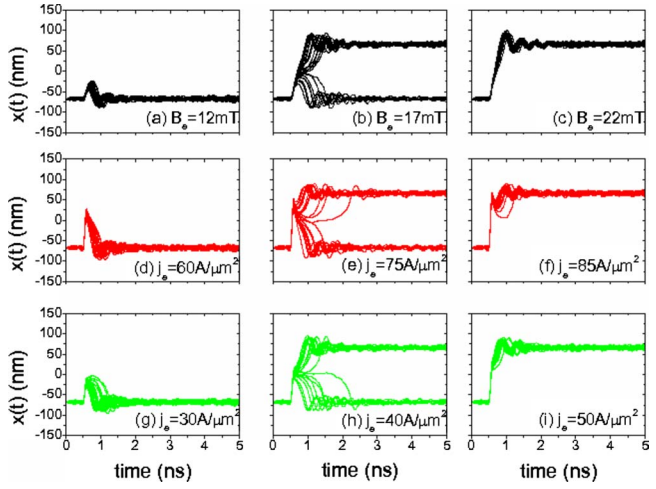

FIG. 14. (Color online) Micromagnetic results at room temperature $T=300$ K of the DW position as a function of time under field pulses of $t_p=100$ ps and different amplitudes: (a) $B_e=12$ mT, (b) $B_e=17$ mT, and (c) $B_e=22$ mT. Graphs (d) $j_a=60$ A/μm^2, (e) $j_a=75$ A/μm^2, and (f) $j_a=85$ A/μm^2 correspond to current pulses in the perfect adiabatic limit ($\xi=0$), whereas (g) $j_a=30$ A/μm^2, (h) $j_a=40$ A/μm^2, and (i) $j_a=50$ A/μm^2 correspond to current pulses considering a nonadiabatic parameter of $\xi=0.04$. The separation is $S=120$ nm, and 25 stochastic realizations are displayed on each graph.

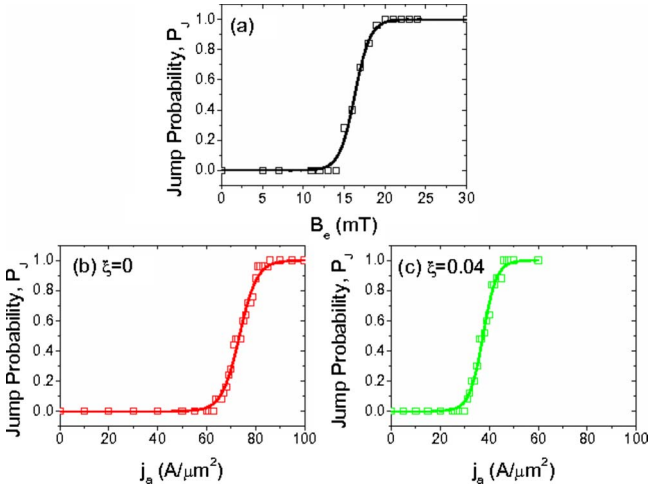

FIG. 15. (Color online) Probability of DW jump from one notch to the other ($S=120$ nm) under pulses of $t_p=100$ ps and different amplitudes: (a) Field pulses, (b) Current pulses in the perfect adiabatic case ($\xi=0$), (c) Current pulses in the nonadiabatic case ($\xi=0.04$). The results were computed by evaluating 25 realizations of the DW dynamics at $T=300$ K. Solid lines correspond to the fittings to $P_J=\{1+\exp[B_e-B_e(T=0\ K)]/\Delta B_e\}^{-1}$ for the field pulses, and $P_J=\{1+\exp[j_a-j_a(T=0\ K)]/\Delta j_a\}^{-1}$ for current pulses.

tion of $S=120$ nm between both pinning sites. The length of the pulses was fixed to $t_p=100$ ps, and several amplitudes, both smaller and larger than the deterministic critical threshold $[B_c(T=0)$ or $j_c(T=0)]$, were evaluated by computing 25 stochastic realizations for each pair of (B_e,t_p) or (j_a,t_p). Figure 14 shows examples of the micromagnetic results, which depict similar features for both field [(a)–(c)], and current pulses with $\xi=0$ [(d)–(f)] and $\xi=0.04$ [(g)–(i)]. The system was evolved freely during the first 0.5 ns of the simulation at room temperature, and then the pulse is applied (at $t=0.5$ ns). For pulses with amplitude smaller than the deterministic critical value $[B_e<B_c(T=0)$ or $j_a<j_c(T=0)$, see the left panel in Fig. 14], the DW does not jump to the right pinning site in any realization. On the contrary, if the amplitude of the pulse is large enough for the critical deterministic threshold $[B_e>B_c(T=0)$ or $j_a>j_c(T=0)$, see the right panel in Fig. 13], the DW jumps to right pinning site occurs with 100% probability. For intermediate amplitudes close to the deterministic threshold (see the central panel in Fig. 14), the DW returns to the initial left pinning site for some realizations but it jumps to the right pinning site for others as due to thermal fluctuations.

The probability of the DW jump (P_J) at $T=300$ K under (a) field and [(b) and (c)] current pulses of constant length ($t_p=100$ ps) is depicted in Fig. 15 as a function of the amplitude. For all cases evaluated the probability of DW jump changes from 0% to 100% in a narrow interval of amplitudes. These results indicate that the writing mechanism for a bistable magnetic random access memory device based on a pinned DW at two different positions could be fast and easily performed by means of short field or current pulses in the subnanosecond regime.

As it was depicted in Fig. 10, the energy barrier E_B between two pinning sites decreases with the separation S. Although it is not shown here, we observed that when two identical pinning sites are separated by $S=30$ nm from each other, the jumps from one pinning site to the other can be induced as due to thermal fluctuations in absence of any driving force. The reason for these jumps is the small energy barrier ($E_B=1.8\times10^{-21}$ J) as compared to the thermal energy, which is $K_BT=4.14\times10^{-21}$ J at room temperature. However, the energy barrier is several times larger than the thermal energy at room temperature for $S=120$ nm (see Sec. VI). It was micromagnetically verified that for this case ($S=120$ nm) the strength of thermal activation by itself (for $B_e=j_a=0$) is not enough to produce the jump of the DW to the adjacent pinning site, and it only fluctuates around the initial pinning site but without jumping outside.

VI. 1DM RESULTS FOR STRIPS WITH TWO PINNING SITES

The results of Secs. IV and V were obtained from a full micromagnetic point of view which considers the three-dimensional (3D) spatial variation in the magnetization. In this section, a one-dimensional approximation is adopted with the aim of describing the DW jumps between two pinning sites which are separated $S=120$ nm from each other. The pinning potential profile is described by the following function

$$V_{\text{pin}}(X)=V_0-V_d\left[\exp\left(-\frac{(X+x_L)^2}{L^2}\right)+\exp\left(-\frac{(X+x_R)^2}{L^2}\right)\right], \quad (5)$$

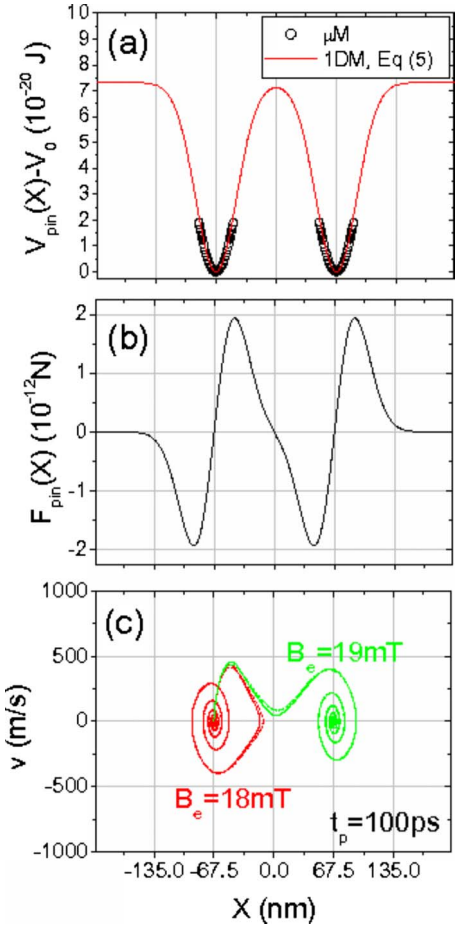

FIG. 16. (Color online) (a) Pinning potential $V_{\mathrm{pin}}(X)$ and (b) pinning force $F_{\mathrm{pin}}(X)$ used to mimic the micromagnetic results of Sec. V by means of the one-dimensional model. (c) Trajectories in the phase space (v vs X) for two field pulses of fixed duration (t_p =100 ps) obtained from 1DM at zero temperature with the following parameters: Δ_0=21.14 nm, N_z=0.8097, and N_y=0.048. Solid lines correspond to the numerical solution of Eq. (A19) considering that the DW width remains constant. Dashed lines were computed from Eqs. (A17) and (A18) and using the dynamical equation for the DW width (Refs. 11 and 64).

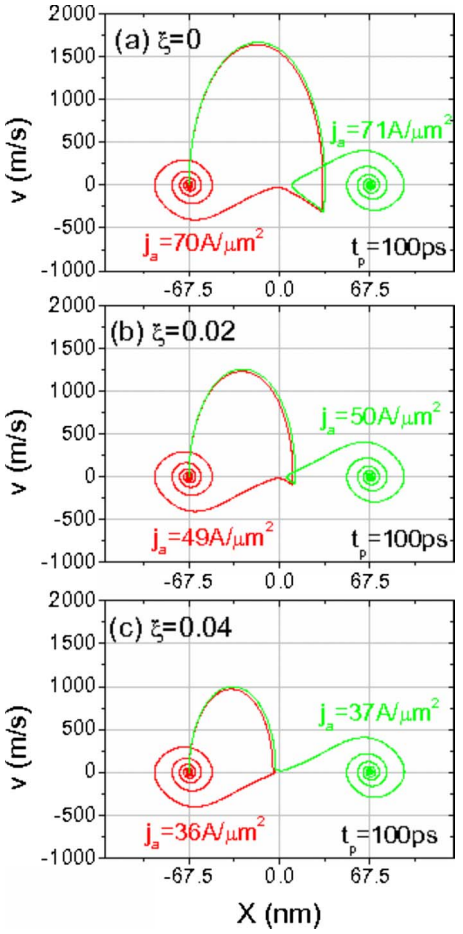

FIG. 17. (Color online) Rigid 1DM trajectories in the phase space (v vs X) for two current pulses of fixed duration (t_p =100 ps). From top to bottom: (a) ξ=0, (b) ξ=0.02, and (c) ξ =0.04.

where V_0 is a constant, x_L=−67.5 nm and x_R=+67.5 nm are the centers for each pinning site, and L and V_d are the length and the effective depth of each pinning site. The values of L and V_d have been estimated by fitting former micromagnetic simulations of Sec. V. For the case of S=120 nm, the following values are inferred: L=32.5 nm and V_d=7.32 $\times 10^{-20}$ J. This energy profile is depicted in Fig. 16(a), where dots correspond to micromagnetic simulations of Fig. 10(d), and solid lines correspond to Eq. (5). The deduced pinning force $F_{\mathrm{pin}}(X)=-\partial V_{\mathrm{pin}}(X)/\partial X$ is also depicted in Fig. 16(b). Taking into account this effective pinning potential in Eq. (A19), the DW dynamics can be numerically solved from a rigid point of view (Δ_0=21.14 nm). Typical rigid 1DM trajectories in the phase space [$v(t)$ vs $X(t)$] are shown in Fig. 16(c) for field pulses of t_p=100 ps (solid lines). The same analysis was also carried out but now it considers that the DW width is a function of time [$\Delta=\Delta(t)$] in both Eqs. (A17) and (A18) (dashed lines). In this case, the dynamical equation which describes the temporal evolution of DW width deduced by Thiaville *et al.*[11,64] was used along with Eqs. (A17) and (A18). In view of the similarity of these results (the curves are almost indistinguishable), we conclude that the temporal evolution of the DW width plays a minor role on the analyzed DW jumps. More importantly, these 1DM results depict similar features with the micromagnetic ones [see Fig. 11(c)].

Figures 17(a)–17(c) show the rigid 1DM trajectories in the phase space [$v(t)$ vs $X(t)$] under current pulses of fixed duration (t_p=100 ps) for three different values of ξ. They depict similar behavior than those obtained from full micromagnetic modeling [see Figs. 12(c) and 13(a)–13(c)].

The critical amplitudes required to promote the DW jumps from the left pinning site to right one as a function of t_p are collected in Fig. 18. The micromagnetic results (μM, dots) are compared with the rigid 1DM predictions (solid lines), and a good quantitative agreement is evidenced. These results indicate that, although the rigid 1DM cannot describe the change in the DW width nor spin waves excitations, it captures the essential aspects of the DW physics, provided

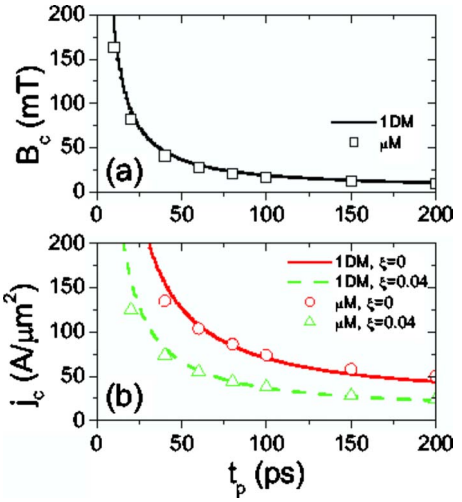

FIG. 18. (Color online) Critical amplitudes of (a) the field (B_c) and (b) density current (j_c) as a function of the pulse duration t_p required to promote the DW jump. Micromagnetic results (μM) are depicted by dots, whereas rigid 1DM predictions are depicted by solid lines.

that the model parameters, such as the effective pinning profile, are suitably chosen based on micromagnetic results.

VII. CONCLUSIONS

In summary, we have presented a micromagnetic analysis of the DW static properties and its motion along thin Permalloy strips driven by short sinusoidal field or current pulses with different amplitudes and durations in the subnanosecond regime. The net DW displacement along perfect strips increases with both the amplitude and the length of the pulses for both field and current pulses if finite nonadiabatic corrections are taken into account, whereas no net displacement is achieved in the perfect adiabatic case. The static properties and the dynamics in strips which contain a single or a double pinning site have been also characterized. In the first case, the analysis of pinning potential indicates that it depends on the size of the constriction. A DW can be moved over distances in the order of several hundreds of nanometers by short pulses but if the distance traveled does not surpass a given threshold when the pulse is turned off, the DW is attracted again to its initial position, which indicates that the pinning potential extends over distances several times larger than the physical size of the constriction. For the strip with two pinning sites, the energy barrier between them can be controlled by their separation. The DW jumps between this bistable system can be achieved by means of short field or current pulses. The critical amplitude of the pulses increases when its duration is reduced for both field and current pulses. The transitions between adjacent pinning sites were also evaluated at room temperature under field or current pulses of constant duration of 100 ps and different amplitudes. The probability of DW jump changes from 0% to 100% in a small range of amplitudes. All these features are attractive for novel magnetic random access memories where a single domain wall could serve as a memory element.

ACKNOWLEDGMENTS

This work was supported by Projects No. MAT2005-04827 and No. MAT2008-04706/NAN from Spanish government, and Projects No. SA063A05 and No. SA025A08 from Junta de Castilla y Leon.

APPENDIX: 1DM

In order to gain analytical insight into the DW dynamics, the 1DM is commonly adopted.[9,24,27] It considers that the magnetization vector $\vec{M}=M_s\vec{m}$ depends only on the axial coordinate x. Denoting by $\theta(x,t)$ the magnetization polar angle (the polar axis being the strip axis), and by $\phi(x,t)$ the azimuthal angle describing the orientation of the magnetization projection on the cross-sectional plane $[\vec{M}=M_s(\cos\theta,\sin\theta\cos\phi,\sin\theta\sin\phi)]$, Eq. (1) reads

$$\dot{\theta}+\alpha\sin\theta\dot{\phi}=\gamma_0 H_{\mathrm{eff},\phi}+b_J\frac{\partial\theta}{\partial x}+c_J\sin\theta\frac{\partial\phi}{\partial x}, \quad \text{(A1)}$$

$$\sin\theta\dot{\phi}-\alpha\dot{\theta}=-\gamma_0 H_{\mathrm{eff},\theta}+b_J\sin\theta\frac{\partial\phi}{\partial x}-c_J\frac{\partial\theta}{\partial x}, \quad \text{(A2)}$$

where the dot notation represents the time derivative ($\dot{\theta}\equiv\partial\theta/\partial t$, $\dot{\phi}\equiv\partial\phi/\partial t$), and the two components of the effective field are

$$H_{\mathrm{eff},\theta}=-\frac{1}{\mu_0 M_s}\frac{\delta\epsilon}{\delta\theta}, \quad \text{(A3)}$$

$$H_{\mathrm{eff},\phi}=-\frac{1}{\mu_0 M_s\sin\theta}\frac{\delta\epsilon}{\delta\phi}, \quad \text{(A4)}$$

where ϵ is the energy density, and $\delta/\delta\Omega$ indicates the functional derivative given by

$$\frac{\delta}{\delta\Omega}=\frac{\partial}{\partial\Omega}-\frac{\partial}{\partial x}\left(\frac{\partial}{\partial\left(\frac{\partial\Omega}{\partial x}\right)}\right) \quad \text{(A5)}$$

for each $\Omega=\theta$ or ϕ.

The energy density ϵ of a free-defect strip consists of four different contributions

$$\epsilon=\epsilon_{\mathrm{ext}}+\epsilon_{\mathrm{ani}}+\epsilon_{\mathrm{exch}}+\epsilon_{\mathrm{dmg}}, \quad \text{(A6)}$$

where the external field $\vec{H}_{\mathrm{ext}}=H_{\mathrm{ext}}\vec{u}_x$ and the uniaxial magnetocrystalline contributions are

$$\epsilon_{\mathrm{ext}}=-\mu_0\vec{M}\cdot\vec{H}_{\mathrm{ext}}=-\mu_0 M_s H_{\mathrm{ext}}\cos\theta, \quad \text{(A7)}$$

$$\epsilon_{\mathrm{ani}}=K_u[1-(\vec{m}\cdot\vec{u}_K)^2]=K_u(1-\cos^2\theta), \quad \text{(A8)}$$

where K_u is the uniaxial magnetocrystalline anisotropy constant and $\vec{u}_K=\vec{u}_x$ is the easy axis. The exchange energy density in the one-dimensional model is given by

$$\epsilon_{\text{exch}} = \frac{A}{M_s^2}\left|\frac{\partial \vec{M}(x)}{\partial x}\right|^2 = A\left[\left(\frac{\partial \theta}{\partial x}\right)^2 + \sin^2\theta\left(\frac{\partial \phi}{\partial x}\right)^2\right], \tag{A9}$$

where A is the exchange constant. The demagnetizing energy density can be expressed as

$$\epsilon_{\text{dmg}} = -\frac{1}{2}\mu_0 \vec{M}\cdot\vec{H}_{\text{dmg}} = \frac{1}{2}\mu_0 M_s^2[N_x\cos^2\theta + (N_y\cos^2\phi + N_z\sin^2\phi)\sin^2\theta], \tag{A10}$$

where the demagnetizing field is assumed to be proportional to the magnetization according to $\vec{H}_{\text{dmg}} = -N\cdot\vec{M}$, with N being a diagonal tensor. Its components N_x, N_y, and N_z are the demagnetizing factors along the x, y, and z directions, respectively, which depend on the strip cross-sectional dimensions.[68]

By placing Eqs. (A7)–(A10) into Eqs. (A3) and (A4), and considering that the DW profile is given by the Walker's trial functions[9,24,27]

$$\phi = \Phi(t), \tag{A11}$$

$$\ln\tan\frac{\theta(x,t)}{2} = \frac{1}{\Delta}[x - X(t)]. \tag{A12}$$

Equations (A1) and (A2) can be written as

$$\frac{\dot{X}}{\Delta} - \alpha\dot{\Phi} = \frac{1}{2}\omega_d\sin(2\Phi) - \frac{b_J}{\Delta}, \tag{A13}$$

$$\dot{\Phi} + \alpha\frac{\dot{X}}{\Delta} = \gamma_0 H_{\text{ext}} - \frac{c_J}{\Delta}, \tag{A14}$$

where $\omega_d = \gamma_0 M_s(N_z - N_y)$ is the angular frequency of magnetization oscillations around the demagnetizing field inside the wall. $X(t)$ represents the DW center position along the x axis. The terms on the right-hand side of Eq. (A14) are related to the driving forces acting on the DW:

$$\gamma_0 H_{\text{ext}} - \frac{c_J}{\Delta} = \frac{\gamma_0}{2\mu_0 M_s L_y L_z}(F_H + F_j),$$

where $F_H = 2\mu_0 M_s L_y L_z H_{\text{ext}}$ is the driving force due to the magnetic field $B_{\text{ext}} = \mu_0 H_{\text{ext}}$, and $F_j = -2\mu_0 M_s L_y L_z c_J/(\gamma_0\Delta)$ is the driving force due to the spin-polarized current with $c_J = \xi b_J$.[69] The DW width Δ is given by

$$\Delta(\Phi) = \left(\frac{A}{K_0 + K\sin^2\Phi}\right)^{1/2}, \tag{A15}$$

where $K_0 = K_u + \frac{1}{2}\mu_0 M_s^2|N_y - N_x|$ and $K = \frac{1}{2}\mu_0 M_s^2(N_z - N_y)$. More details on how Eqs. (A13)–(A15) are obtained can be found in Ref. 24.

Equations (A13) and (A14) describe the DW dynamics along perfect strips.[27,64,67] In order to include the effect of notches which act as a trap for the DW position, the external field H_{ext} has to be replaced by $H_{\text{ext}} + H_{\text{pin}}(X)$, where $H_{\text{pin}}(X)$ represents the pinning field, which is derived from the pinning potential $V_{\text{pin}}(X)$ as

$$H_{\text{pin}}(X) = -\frac{1}{2\mu_0 M_s L_y L_z}\frac{\partial V_{\text{pin}}(X)}{\partial X}. \tag{A16}$$

Introducing this pinning field $H_{\text{pin}}(X)$, Eqs. (A13) and (A14) can be written as

$$(1+\alpha^2)\frac{\dot{X}}{\Delta} = \alpha\gamma_0 H_{\text{ext}} - \alpha\frac{\gamma_0}{2\mu_0 M_s L_y L_z}\frac{\partial V_{\text{pin}}(X)}{\partial X} + \frac{1}{2}\omega_d\sin(2\Phi) - (1+\alpha\xi)\frac{b_J}{\Delta}, \tag{A17}$$

$$(1+\alpha^2)\dot{\Phi} = \gamma_0 H_{\text{ext}} - \frac{\gamma_0}{2\mu_0 M_s L_y L_z}\frac{\partial V_{\text{pin}}(X)}{\partial X} - \alpha\frac{1}{2}\omega_d\sin(2\Phi) - (\xi - \alpha)\frac{b_J}{\Delta}, \tag{A18}$$

which are analogous to the rigid one-dimensional equations used in Refs. 52 and 55.

Former Eqs. (A17) and (A18) describe the DW dynamics under both magnetic fields and/or spin-polarized currents from the one-dimensional point of view, where it is given by the DW center position X and the tilt angle Φ. Considering that DW width remains constant with respect to its static value ($\Delta = \Delta_0$), and that the tilt angle is small (typically, $\Phi < 10°$), Eqs. (A17) and (A18) can be linearized, and the following equation is obtained

$$(1+\alpha^2)\frac{d^2X}{dt^2} + \eta\frac{dX}{dt} + \frac{1}{m_w}\frac{\partial V_{\text{pin}}(X)}{\partial X} = f(t), \tag{A19}$$

where $m_w = 2(\mu_0 L_y L_z)/\gamma_0^2(N_z - N_y)\Delta_0$ is the effective DW mass, and the friction coefficient η is given by

$$\eta = \alpha\omega_d\left(1 + \frac{1}{m_w\omega_d^2}\frac{\partial^2 V_{\text{pin}}(X)}{\partial X^2}\right). \tag{A20}$$

The term on the right-hand side of Eq. (A19) $[f(t)]$ represents the total external (or driving) force per unit of mass m_w, which can be written as the sum of both static and dynamics, and field and current contributions $[f(t) = f_{H,s} + f_{H,d} + f_{j,s} + f_{j,d}]$. Under time-varying field $[B_{\text{ext}}(t) = \mu_0 H_{\text{ext}}(t)]$, $f(t)$ is given by

$$f(t) = f_{H,s} + f_{H,d} = \gamma_0\Delta_0\omega_d H_{\text{ext}} + \alpha\gamma_0\Delta_0\frac{\partial H_{\text{ext}}(t)}{\partial t}, \tag{A21}$$

whereas for current pulses $[j_{\text{app}}(t)]$, the instantaneous driving force per unit of mass is

$$f(t) = f_{j,s} + f_{j,d} = -\xi\omega_d\frac{\mu_B P}{eM_s}j_{\text{app}}(t) - (1+\alpha\xi)\frac{\mu_B P}{eM_s}\frac{\partial j_{\text{app}}(t)}{\partial t}. \tag{A22}$$

Considering the case of perfect strips $[V_{\text{pin}}(X) = 0]$, the DW velocity under field $B_{\text{ext}}(t)$ or current $j_{\text{app}}(t)$ pulses with

sinusoidal form [where $B_{\mathrm{ext}}(t)=B_e \sin(\pi t/t_p)$ if $0\le t\le t_p$, and $B_{\mathrm{ext}}(t)=0$ if $t\ge t_p$] can analytically be obtained by solving Eq. (A19). For $0\le t\le t_p$, the instantaneous velocity $[\dot{X}(t)\equiv v(t)]$ is given by

$$v_\beta(t)=A_\beta\left\{B_\beta\left[e^{-(\alpha\omega_d t/1+\alpha^2)}-\cos\left(\frac{\pi t}{t_p}\right)\right]+C_\beta\sin\left(\frac{\pi t}{t_p}\right)\right\}, \tag{A23}$$

where $\beta: H,j$ for field and current pulses, respectively. For field pulses ($\beta=H$), the coefficients A_H, B_H, and C_H are given by

$$A_H=\frac{\gamma_0\Delta_0 H_e t_p}{[(\alpha\omega_d t_p)^2+\pi^2(1+\alpha^2)^2]}, \tag{A24}$$

$$B_H=\pi\omega_d, \tag{A25}$$

$$C_H=\alpha\left(\omega_d^2 t_p+\frac{\pi^2}{t_p}(1+\alpha^2)\right), \tag{A26}$$

whereas for current pulses ($\beta=j$),

$$A_j=-\frac{\mu_B P}{eM_s}\frac{j_a t_p}{[(\alpha\omega_d t_p)^2+\pi^2(1+\alpha^2)^2]}, \tag{A27}$$

$$B_j=\pi\omega_d(\xi-\alpha), \tag{A28}$$

$$C_j=\alpha\xi\left(\omega_d^2 t_p+\frac{\pi^2}{t_p}(1+\alpha^2)\right)+\frac{\pi^2}{t_p}(1+\alpha^2). \tag{A29}$$

The instantaneous DW position during the pulse ($0\le t\le t_p$) is

$$X_\beta(t)=A_\beta B_\beta\left[\frac{1+\alpha^2}{\alpha\omega_d}(1-e^{-(\alpha\omega_d t/1+\alpha^2)})-\frac{t_p}{\pi}\sin\left(\frac{\pi t}{t_p}\right)\right]+A_\beta C_\beta\left(\frac{t_p}{\pi}\right)\left[1-\cos\left(\frac{\pi t}{t_p}\right)\right]. \tag{A30}$$

On the other hand, the DW velocity after the pulse is turned off [for $t\ge t_p$, $B_{\mathrm{ext}}(t)=j_{\mathrm{app}}(t)=0$] is given by

$$v_\beta(t)=v_\beta(t_p)e^{-[\alpha\omega_d(t-t_p)/1+\alpha^2]}, \tag{A31}$$

where $v_\beta(t_p)$ is the velocity of the DW at the end of the pulse. The DW position for $t\ge t_p$ can be obtained by integration from Eq. (A31),

$$X_\beta(t)=X_\beta(t_p)+v_\beta(t_p)\frac{1+\alpha^2}{\alpha\omega_d}(1-e^{-[\alpha\omega_d(t-t_p)/1+\alpha^2]}), \tag{A32}$$

where $X_\beta(t_p)$ is the position of the DW center at the end of the pulse.

The effect of thermal flluctuations is included in the 1DM by replacing H_{ext} by $H_{\mathrm{ext}}+H_{\mathrm{th}}(t)$ in both Eqs. (A17) and (A18). The stochastic random thermal field $H_{\mathrm{th}}(t)$ is assumed to be a Gaussian-distributed stochastic process with zero mean value $[\langle H_{\mathrm{th}}(t)\rangle=0]$ and uncorrelated in time $[\langle H_{\mathrm{th}}(t)H_{\mathrm{th}}(t')\rangle=2D\delta(t-t')]$. The factor D represents the strength of the thermal field, which can be obtained from the fluctuation-dissipation theorem ($D=\sqrt{\frac{\alpha K_B T}{\mu_0 V_{\mathrm{DW}}\gamma_0 M_s}}$, where $V_{\mathrm{DW}}=\Delta L_y L_z$ is the volume of the DW). On the other hand, thermal fluctuations enter in the linearized 1DM by adding a thermal force (per unit of mass) on the right hand side of Eq. (A19), as was described in Ref. 16.

*Corresponding author; emvecino@ubu.es

[1] S. S. P. Parkin, U.S. Patent No. 6834005 (16 December 2004).
[2] J. A. Drewes, U.S. Patent No. 7034374 (25 April 2006).
[3] S. H. Chung and A. F. Hoffmann, U.S. Patent No. 7042036 (9 May 2006).
[4] S. E. Barnes, J. Ieda, and S. Maekawa, Appl. Phys. Lett. **89**, 122507 (2006).
[5] C. Chappert, A. Fert, and F. Nguyen Van Dau, Nature Mater. **6**, 813 (2007).
[6] D. Atkinson, D. S. Eastwood, and L. K. Bogart, Appl. Phys. Lett. **92**, 022510 (2008).
[7] D. Allwood, G. Xiong, M. D. Cooke, C. C. Faulkner, D. Atkinson, N. Vernier, and R. P. Cowburn, Science **296**, 2003 (2002); D. A. Allwood, G. Xiong, C. C. Faulkner, D. Atkinson, D. Petit, and R. P. Cowburn, *ibid.* **309**, 1688 (2005).
[8] P. Xu, K. Xia, C. Gu, L. Tang, H. Yang, and J. Li, Nat. Nanotechnol. **3**, 97 (2008).
[9] N. L. Schryer and L. R. Walker, J. Appl. Phys. **45**, 5406 (1974).
[10] R. D. McMichael and M. J. Donahue, IEEE Trans. Magn. **33**, 4167 (1997).
[11] A. Thiaville, J. M. Garcia, and J. Miltat, J. Magn. Magn. Mater. **242-245**, 1061 (2002).
[12] Y. Nakatani, A. Thiaville, and J. Miltat, Nature Mater. **2**, 521 (2003).
[13] D. Atkinson, D. A. Allwood, G. Xiong, M. D. Cooke, and R. P. Cowburn, Nature Mater. **2**, 85 (2003).
[14] D. G. Porter and M. J. Donahue, J. Appl. Phys. **95**, 6729 (2004).
[15] G. S. D. Beach, C. Nistor, C. Knutson, M. Tsoi, and J. L. Erskine, Nature Mater. **4**, 741 (2005).
[16] E. Martinez, L. Lopez-Diaz, L. Torres, C. Tristan, and O. Alejos, Phys. Rev. B **75**, 174409 (2007).
[17] L. Berger, Phys. Lett. **46A**, 3 (1973).
[18] L. Berger, J. Appl. Phys. **49**, 2156 (1978).
[19] L. Berger, J. Appl. Phys. **55**, 1954 (1984).
[20] J. Slonczewski, J. Magn. Magn. Mater. **159**, L1 (1996).
[21] J. Slonczewski, J. Magn. Magn. Mater. **195**, 261 (1999).
[22] Ya. B. Bazaliy, B. A. Jones, and Shou-Cheng Zhang, Phys. Rev. B **57**, R3213 (1998).
[23] G. Tatara and H. Kohno, Phys. Rev. Lett. **92**, 086601 (2004).
[24] Z. Li and S. Zhang, Phys. Rev. B **70**, 024417 (2004).
[25] S. Zhang and Z. Li, Phys. Rev. Lett. **93**, 127204 (2004).
[26] A. Thiaville, Y. Nakatani, J. Miltat, and N. Vernier, J. Appl. Phys. **95**, 7049 (2004).
[27] A. Thiaville, Y. Nakatani, J. Miltat, and S. Suzuki, Europhys.

Lett. **69**, 990 (2005).
[28] S. E. Barnes and S. Maekawa, Phys. Rev. Lett. **95**, 107204 (2005).
[29] Z. Li, J. He, and S. Zhang, J. Appl. Phys. **99**, 08Q702 (2006).
[30] J. He, Z. Li, and S. Zhang, J. Appl. Phys. **99**, 08G509 (2006).
[31] Y. Tserkovnyak, H. J. Skadsem, A. Brataas, and G. E. W. Bauer, Phys. Rev. B **74**, 144405 (2006).
[32] G. Tatara, T. Takayama, H. Kohno, J. Shibata, Y. Nakatani, and H. Fukuyama, J. Phys. Soc. Jpn. **75**, 064708 (2006).
[33] R. A. Duine, A. S. Nunez, and A. H. MacDonald, Phys. Rev. Lett. **98**, 056605 (2007).
[34] J. Grollier, P. Boulenc, V. Cros, A. Hamzic, A. Vaures, and A. Fert, Appl. Phys. Lett. **83**, 509 (2003).
[35] M. Klaui, P. O. Jubert, R. Allenspach, A. Bischof, J. A. C. Bland, G. Faini, U. Rudiger, C. A. F. Vaz, L. Vila, and C. Vouille, Phys. Rev. Lett. **95**, 026601 (2005).
[36] M. Laufenberg, W. Buhrer, D. Bedau, P. E. Melchy, M. Klaui, L. Vila, G. Faini, C. A. F. Vaz, J. A. C. Bland, and U. Rudiger, Phys. Rev. Lett. **97**, 046602 (2006).
[37] M. Hayashi, L. Thomas, Ya. B. Bazaliy, C. Rettner, R. Moriya, X. Jiang, and S. S. P. Parkin, Phys. Rev. Lett. **96**, 197207 (2006).
[38] G. S. D. Beach, C. Knutson, C. Nistor, M. Tsoi, and J. L. Erskine, Phys. Rev. Lett. **97**, 057203 (2006).
[39] G. Meier, M. Bolte, R. Eiselt, B. Kruger, Dong-Hyun Kim, and P. Fischer, Phys. Rev. Lett. **98**, 187202 (2007).
[40] S. Laribi, V. Cros, V. Munoz, J. Grollier, A. Hamzic, G. Deranlot, A. Fert, E. Martinez, L. Lopez-Diaz, L. Villa, G. Faini, S. Zoll, and R. Fournel, Appl. Phys. Lett. **90**, 232505 (2007).
[41] L. Heyne, M. Klaui, D. Backes, P. Monhrke, T. A. Moore, J. G. Kimling, O. Boulle, and U. Rudinger, J. Appl. Phys. **103**, 07D928 (2008).
[42] F. Junginger, M. Kläui, D. Backes, U. Rüdiger, T. Kasama, R. E. Dunin-Borkowskid, L. J. Heyderman, C. A. F. Vaz, and J. A. C. Bland, Appl. Phys. Lett. **90**, 132506 (2007).
[43] G. S. D. Beach, M. Tsoi, and J. L. Erskine, J. Magn. Magn. Mater. **320**, 1272 (2008).
[44] Y. Tserkovnyak, A. Brataas, and G. E. W. Bauer, J. Magn. Magn. Mater. **320**, 1282 (2008).
[45] M. Klaui, C. A. F. Vaz, J. Rothman, J. A. C. Bland, W. Wernsdorfer, G. Faini, and E. Cambril, Phys. Rev. Lett. **90**, 097202 (2003).
[46] C. C. Faulkner, M. D. Cooke, D. A. Allwood, D. Petit, D. Atkinson, and R. P. Cowburn, J. Appl. Phys. **95**, 6717 (2004).
[47] J. Grollier, D. Lacour, V. Cros, A. Hamzic, A. Vaures, A. Fert, D. Adam, and G. Faini, J. Appl. Phys. **92**, 4825 (2002).
[48] M. Tsoi, R. E. Fontana, and S. S. P. Parkin, Appl. Phys. Lett. **83**, 2617 (2003).
[49] M. Klaui, C. A. F. Vaz, J. A. C. Bland, W. Wernsdorfer, G. Faini, E. Cambril, L. J. Heyderman, F. Nolting, and U. Rudiger, Phys. Rev. Lett. **94**, 106601 (2005).
[50] D. Ravelosona, D. Lacour, J. A. Katine, B. D. Terris, and C. Chappert, Phys. Rev. Lett. **95**, 117203 (2005).
[51] M. Hayashi, L. Thomas, C. Rettner, R. Moriya, X. Jiang, and S. S. P. Parkin, Phys. Rev. Lett. **97**, 207205 (2006).
[52] L. Thomas, M. Hayashi, X. Jiang, R. Moriya, C. Rettner, and S. S. P. Parkin, Nature (London) **443**, 197 (2006).
[53] P. Dagras, M. Klaui, M. Laufenberg, D. Bedau, L. Vila, G. Faini, C. A. F. Vaz, J. A. C. Bland, and U. Rudinger, J. Phys. D **40**, 1247 (2007).
[54] E. Martinez, L. Lopez-Diaz, O. Alejos, L. Torres, and C. Tristan, Phys. Rev. Lett. **98**, 267202 (2007).
[55] L. Thomas, M. Hayashi, X. Jiang, R. Moriya, C. Rettner, and S. S. P. Parkin, Science **315**, 1553 (2007).
[56] T. Nozaki, H. Maekawa, M. Mizuguchi, M. Shiraishi, T. Shinjo, Y. Suzuki, H. Maehara, S. Kasai, and T. Ono, Appl. Phys. Lett. **91**, 082502 (2007).
[57] D. Bedau, M. Klaui, S. Krzyk, U. Rudiger, G. Faini, and L. Vila, Phys. Rev. Lett. **99**, 146601 (2007).
[58] E. Saitoh, H. Miyajima, T. Yamaoka, and G. Tatara, Nature (London) **432**, 203 (2004).
[59] G. Tatara, E. Saitoh, M. Ichimura, and H. Kohno, Appl. Phys. Lett. **86**, 232504 (2005).
[60] Peng-Bin He, X. C. Xie, and W. M. Liu, Phys. Rev. B **72**, 172411 (2005).
[61] E. Martinez, L. Lopez-Diaz, O. Alejos, and L. Torres, Phys. Rev. B **77**, 144417 (2008).
[62] W. F. Brown, Phys. Rev. **130**, 1677 (1963).
[63] J. L. Garcia-Palacios and F. J. Lazaro, Phys. Rev. B **58**, 14937 (1998).
[64] A. Thiaville and Y. Nakatani, *Spin Dynamics in Confined Magnetic Structures III* (Springer, Berlin, 2006), pp. 161–206.
[65] M. Hayashi, L. Thomas, C. Rettner, R. Moriya, and S. S. P. Parkin, Nat. Phys. **3**, 21 (2007).
[66] M. Hayashi, L. Thomas, C. Rettner, R. Moriya, and S. S. P. Parkin, Appl. Phys. Lett. **92**, 162503 (2008).
[67] A. Thiaville, Y. Nakatani, F. Piechon, J. Miltat, and T. Ono, Eur. Phys. J. B **60**, 15 (2007).
[68] A. Aharoni, J. Appl. Phys. **83**, 3432 (1998).
[69] As proposed by Tatara and Kohno (Ref. 23), there are other possible contributions to the current-driving force, which is proportional to the DW resistance R_{DW}, $F_j = enR_{\mathrm{DW}}IL_yL_z$, where $n \approx a^{-3}$ is the electron density (a is the lattice constant), and $I = j_a L_y L_z$ is the current. It easy to verify that, if both contributions are taken into account, the current-driving force can be expressed as $F_j = -2\mu_0 M_s L_y L_z c_J'/(\gamma_0 \Delta)$, where $c_J' \equiv \mu_B(\xi P + \tilde{R})/(eM_s)$ and $\tilde{R} = \Delta e^2 n R_{\mathrm{DW}} L_y L_z$ is the dimensionless DW resistivity. This additional term (proportional to $\tilde{R}$) will be omitted unless the contrary is said.